



Energy Density Comparison of Li-ion Cathode Materials Using Dimensional Analysis

Wenbo Du,^{a,*} Nansi Xue,^a Ann M. Sastry,^b Joaquim R. R. A. Martins,^a and Wei Shyy^{a,c,z}

^aDepartment of Aerospace Engineering, University of Michigan, Ann Arbor, Michigan 48109, USA

^bDepartment of Mechanical Engineering, University of Michigan, Ann Arbor, Michigan 48109, USA

^cDepartment of Mechanical Engineering, Hong Kong University of Science and Technology, Clear Water Bay, Hong Kong

A surrogate modeling framework is implemented to analyze the performance of a Li-ion cell with respect to four input variables: cycling rate, particle size, diffusivity, and electrical conductivity. Five different cathode materials (LiMn_2O_4 , LiFePO_4 , LiCoO_2 , $\text{LiV}_6\text{O}_{13}$, and LiTiS_2) are modeled, and ranges for all material properties are selected based on reported data from the literature. The relative impact of the variables is quantified using global sensitivity analysis, and critical diffusivity and conductivity values are calculated. Two dimensionless parameters based on relative time and conductivity scales are defined and found to separate operating conditions into distinct regimes in which the cell performance is limited by diffusion or conduction. Combining the two dimensionless parameters into a single quantity and non-dimensionalizing the energy performance yields a Pareto-efficient set of solutions that are described well by the generalized logistic function, which can be considered a reduced-order model of battery performance with a global analytical solution.

© 2013 The Electrochemical Society. [DOI: 10.1149/2.069308jes] All rights reserved.

Manuscript submitted February 12, 2013; revised manuscript received April 18, 2013. Published May 18, 2013.

Lithium-ion batteries have attracted significant interest in recent years due to their high achievable energy and power density, making them ideal for a wide range of applications. Improving the design of batteries to realize maximum energy and power performance requires an understanding of how variables such as diffusivity, conductivity, and particle size influence the cell behavior. The problem is complicated by the wide ranges in the data reported for these variables due to differences in measurement techniques and sample preparation procedures. Additionally, there are a large number of materials suitable for use in electrodes,¹ and in most applications a range of C-rates must be considered to account for different operating conditions. Since parametric sweeps that sequentially vary one parameter at a time are inefficient and unable to account for nonlinear interactions between parameters, a systematic method for simultaneously studying multiple variables is necessary for complicated multi-physics problems such as the coupled electrochemical and transport processes in a lithium-ion cell.

Through various experimental and numerical studies, cell performance has been found to depend strongly on a large number of operational, morphological, and material-dependent parameters. For example, the effects of particle size^{2,3} and cycling rate⁴ on capacity have been quantified using various experimental techniques, while simulations have been used to quantify the impact of particle size and diffusivity on cell performance.⁵ Simulations have also been used to show that a uniform size distribution can maximize capacity under different cycling rates.⁶ Progress has also been made in studying the evolution of material properties, such as that resulting from the introduction of conductive additives.⁷ However, the measurements and analysis in each of these studies were conducted for a single cathode material and do not offer a comparison between candidate materials that accounts for differences in material properties. Studies comparing multiple materials often focus on specific properties such as overcharge behavior⁸ or thermal stability,⁹ and not on the overall cell performance. Howard and Spotnitz¹⁰ have conducted a comparison of the cell-level performance of various cathode materials that does not consider the effects of transport coefficients or particle size. Dimensional analysis has been applied by Doyle and Newman¹¹ to derive analytical solutions to characterize battery performance based on operating parameters. Three solutions based on different limiting phenomena were obtained, but a single global analysis without simplified physics is still missing.

Despite recent progress in understanding the relevant physical processes in lithium-ion cells, there remains a need for a systematic com-

parison of several candidate materials under a wide range of cycling conditions, and in the presence of significant uncertainty in material properties. In particular, a proper analysis of cell performance must account for both the diffusivity and the conductivity of the materials.¹ In order to address this issue, we define two objectives in this work: to identify critical diffusivity and conductivity levels for achieving high energy density with several different cathode materials, and to establish the relationship between the cell performance and material properties by applying dimensional analysis techniques that combine multiple physical variables to obtain relevant dimensionless transport parameters. Realizing these objectives requires a suitable mathematical framework capable of efficiently relating the outputs of a lithium-ion cell model to its inputs. A good option is the surrogate modeling framework, which builds approximate (surrogate) functions from pre-computed model simulations to significantly reduce the computational time required for additional function evaluations within the parameter space.¹² The surrogate modeling framework has been applied to various engineering problems, including the study of intercalation-induced stress on single lithium manganese oxide particles,¹³ and the effect of microstructure on the transport and reaction properties of particle clusters.¹⁴

In the present study, the output function of interest is the gravimetric energy density, also known as the mass-specific energy density or simply “specific energy”. The input variables are the cycling rate, the size of solid particles in the cathode, and the diffusion coefficient and electrical conductivity of the solid cathode material. Five different cathode materials are considered: lithium manganese oxide (LiMn_2O_4), lithium iron phosphate (LiFePO_4), lithium cobalt oxide (LiCoO_2), lithium vanadium oxide ($\text{LiV}_6\text{O}_{13}$), and lithium titanium sulfide (LiTiS_2). Separate model simulations and surrogate-based analyses are conducted for each material, although the same design of experiments is used to ensure consistent sampling within the parameter space. Since the focus of this work is on comparing cathode materials, the electrolyte (1 M LiPF_6 in EC:DMC) and anode material (MCMB graphite) remain the same for each set of analyses. Ranges for all variables are selected based on values reported in the literature for the corresponding material.

Methodology

Battery cell model and relevant dimensions.— In this study, a single discharge of a cell consisting of a cathode-electrolyte-anode system is modeled using the porous electrode formulation with concentrated solution theory.¹⁵ A schematic of the cell configuration considered in this model is shown in Figure 1. The computational domain consists of two separate dimensions, each with a corresponding length

*Electrochemical Society Student Member.

^zE-mail: weishyy@ust.hk

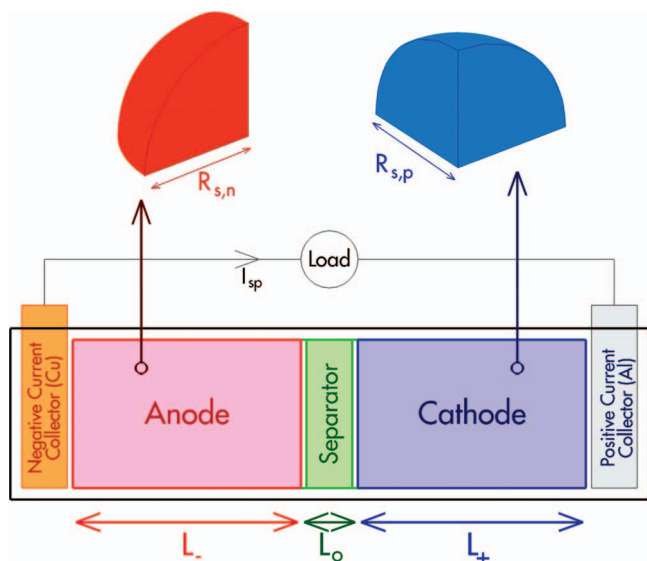


Figure 1. Configuration of a battery cell showing the cathode thickness L_+ and particle radius $R_{s,p}$.

scale. An axial dimension across the thickness of the cell models the electric potential distribution in the solid and liquid phases via Eqs. 1 and 2, respectively.

$$\nabla \cdot (\sigma^{\text{eff}} \nabla \varphi_1) - J = 0 \quad [1]$$

$$\nabla \cdot (\kappa^{\text{eff}} \nabla \varphi_2) + \nabla \cdot (\kappa_D \nabla (\ln c_2)) + J = 0 \quad [2]$$

The effective transport coefficients σ^{eff} and κ^{eff} are calculated from bulk properties using a Bruggeman correction to account for electrode porosity. As indicated in Figure 1, the relevant length scales for the electron and ion conduction processes are the electrode and separator thicknesses, denoted L_- for the anode, L_+ for the cathode, and L_0 for the separator. The axial dimension also models lithium ion diffusion in the liquid phase using Eq. 3.

$$\varepsilon_2 \frac{\partial c_2}{\partial t} = \nabla \cdot (D_2^{\text{eff}} \nabla c_2) + \frac{1 - t_+^0}{F} \nabla \cdot \mathbf{i}_2 - \frac{\mathbf{i}_2 \cdot \nabla t_+^0}{F} \quad [3]$$

A second radial dimension models the effect of particle size on the lithium ion distribution within the electrodes by calculating the time-dependent ion concentration distribution within spherical particles using Eq. 4.

$$\frac{\partial c_1}{\partial t} = \frac{1}{r^2} \frac{\partial}{\partial r} \left(D_s r^2 \frac{\partial c_1}{\partial r} \right) \quad [4]$$

The length scale for the radial dimension is the particle radius, denoted $R_{s,n}$ for the anode and $R_{s,p}$ for the cathode. For the dimensional analysis performed in this study, it is important to use the correct length scale when deriving dimensionless parameters associated with conduction and diffusion.

Note that radial diffusion equation is solved at each axial computational node in the electrodes, but not the electrolyte which contains no active solid. The axial and radial dimensions are coupled via the Butler-Volmer equation for electrochemical kinetics at the solid-liquid interface. Although this formulation cannot resolve the detailed microstructure of the electrode materials due to homogenization, it has the advantage of being computationally inexpensive, and has thus been commonly used as a method for studying cell performance.¹⁶ The computational efficiency allows us to conduct a large number of simulations to examine the large parameter space. Further details of the battery cell model have been summarized by Doyle et al.¹⁵

Surrogate modeling framework.—The surrogate modeling process is illustrated in Figure 2. The following is a brief overview of

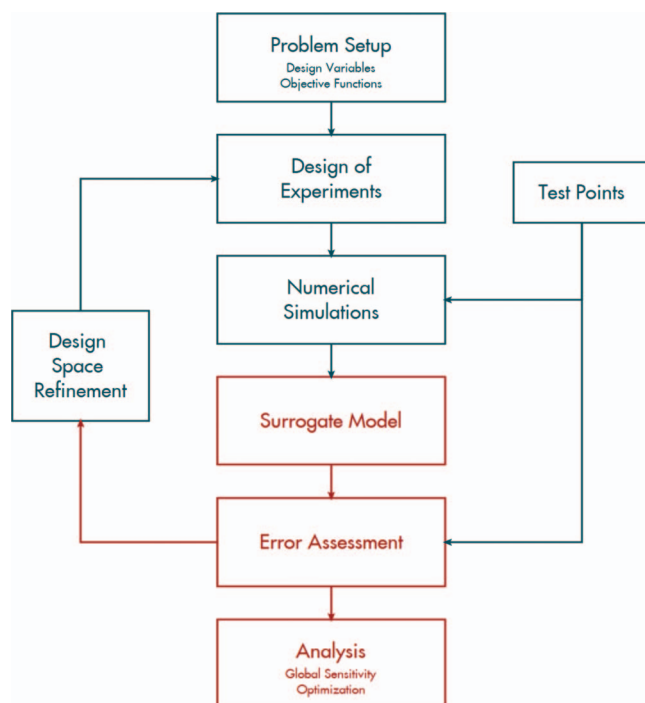


Figure 2. Schematic of surrogate modeling framework. Processes in red are part of the MATLAB surrogates toolbox.

the key steps to this process; further details have been provided by Queipo et al.¹⁷

Once the design variables and objective functions have been defined, the next step requires performing a design of experiments to select the simulations to be used for building the surrogate models.

Design of Experiments.—The design of experiments consists of the set of inputs to the battery cell simulations from which simulation data will be obtained to train the surrogate models. To capture data at the extremities of the design space while ensuring an unbiased sampling of the full range of each design variable, an approach combining face-centered composite design (FCCD)¹⁸ and Latin hypercube sampling (LHS)¹⁹ points is employed in this study.

Surrogate Model Construction.—The data obtained from the design of experiments are used to construct surrogate models that make use of regression and interpolation techniques to approximate the objective function within the full design space. There are many types of surrogate modeling strategies available; in this study we consider polynomial response surface (PRS), kriging (KRG), and radial basis neural network (RBNN) models. The PRS models consist of a linear combination of polynomial basis functions, whose coefficients are determined using a least-squares regression approach. The KRG models consist of a combination of low-order polynomial regression and correlation functions based on the distance from training data points in the design space.²⁰ The RBNN models approximate the objective function as a linear combination of Gaussian radial basis functions.²¹

Error Assessment.—Error measures are necessary to validate the surrogate models. Two error assessment strategies are used in this study: prediction error sum of squares (PRESS), and independent test data. PRESS is the sum of “leave-one-out” errors, which are the errors between the true data values and those predicted from a reconstructed surrogate from all other data points from the design of experiments. Although PRESS values do not require additional data, they can be expensive to compute if the design of experiments contains a large number of data points, and may not necessarily be representative of the true error if the number of data points is small, since the surrogate model is constructed from a different design of experiments. In addition to PRESS, prediction errors at independent test points are also

Table I. Variables and ranges.

Variable	Minimum	Maximum	References
Cycling rate	C/10	10C	
LiMn ₂ O ₄			
Particle size	5.0 μm	15 μm	25
Diffusivity	$1.0 \times 10^{-15} \text{ m}^2/\text{s}$	$1.0 \times 10^{-12} \text{ m}^2/\text{s}$	26–28
Conductivity	$1.0 \times 10^{-6} \text{ S/m}$	10 S/m	29, 30
LiFePO ₄			
Particle size	0.02 μm	8.0 μm	31
Diffusivity	$1.0 \times 10^{-14} \text{ m}^2/\text{s}$	$1.0 \times 10^{-11} \text{ m}^2/\text{s}$	32, 33
Conductivity	$1.0 \times 10^{-5} \text{ S/m}$	10 S/m	32, 34
LiCoO ₂			
Particle size	0.03 μm	6.0 μm	35
Diffusivity	$1.6 \times 10^{-17} \text{ m}^2/\text{s}$	$1.0 \times 10^{-11} \text{ m}^2/\text{s}$	36–38
Conductivity	20 S/m	$5.0 \times 10^4 \text{ S/m}$	39
LiV ₆ O ₁₃			
Particle size	1.0 μm	25 μm	40, 41
Diffusivity	$5.0 \times 10^{-13} \text{ m}^2/\text{s}$	$3.5 \times 10^{-12} \text{ m}^2/\text{s}$	42
Conductivity	$1.0 \times 10^{-3} \text{ S/m}$	$1.0 \times 10^{-2} \text{ S/m}$	42
LiTiS ₂			
Particle size	0.1 μm	10 μm	
Diffusivity	$4.0 \times 10^{-17} \text{ m}^2/\text{s}$	$5.6 \times 10^{-13} \text{ m}^2/\text{s}$	43
Conductivity	5.0 S/m	33.3 S/m	43, 44

computed. The selection of these points requires a separate design of experiments and simulation data. Additional validation criteria are also available for regression-based models like PRS, such as the coefficient of determination (R^2) and adjusted coefficient of determination (R^2_{adj}).

Global Sensitivity Analysis.—The relative magnitudes of impact each input variable has on the objective function can be compared using global sensitivity analysis. An approach similar to that developed by Sobol is implemented in this study.²² A five-point Gauss quadrature method is applied to the surrogate model to compute measures of the relative sensitivity of the objective function to each input variable, known as sensitivity indexes. For simplicity, only the main sensitivity index, which captures the first-order effects, is considered in this study.

Results

Problem setup.—As mentioned previously, the variables serving as inputs to the surrogate model are the particle size, diffusivity, and conductivity of each cathode material, as well as the C-rate. The ranges considered in this study are summarized in Table I, along with appropriate references. No literature on the size of LiTiS₂ particles was available, so bounds were selected to capture a wide range of scenarios. Since the parameter ranges span several orders of magnitude in many cases, a base-10 logarithmic transformation is used to convert between the dimensionless sampling variables and physical variables in the design of experiments. An advantage of the surrogate modeling approach is that interdependencies among the parameters are automatically captured by mapping the global parameter space, and the surrogate models are able to separate first-order effects from higher-order cross-effects. Therefore, there is no need to model the effects of particle size on volume fractions or transport coefficients.

Additional material properties for the cathode materials are listed in Table II, and fixed parameter values for the cell simulations in Table III. Open circuit voltages for LiV₆O₁₃, LiFePO₄, and LiMn₂O₄ are taken from refs. 15, 23, 24, while those for the other materials are found in the database in version 5.1 of the dualfoil program. In all cases the electrolyte is 1 molar LiPF₆ in EC:DMC and the inert filler is PVDF.

Note that since identical values for the volume fraction of all phases and thickness of the electrodes are used in all simulations, the total capacity in the two electrodes is not balanced. Since the objective of this work is to analyze and compare different materials rather than to

Table II. Electrode material properties.

Material	Density (kg/m ³)	Specific capacity (mAh/g)	Cut-off voltage (V)
LiMn ₂ O ₄	4280	148	3.0
LiFePO ₄	3580	170	3.0
LiCoO ₂	5010	274	3.0
LiV ₆ O ₁₃	3900	417	1.8
LiTiS ₂	2285	225	1.6
LiC ₆	2260	372	-

optimize the cell, the electrodes can be unbalanced for consistency in numerical analysis.

The output function of interest is the energy density, which is computed by time-integrating the cell voltage curve obtained from solving the governing equations, and multiplying by the discharge current and other appropriate constants to obtain the total energy provided during the discharge simulation. This value is then converted to mass-specific energy density by dividing by the combined mass of the active and inactive solid, liquid, and current collectors.

Global sensitivity analysis.—A single design of experiments in dimensionless variables consisting of 1296 points in a Latin hypercube sampling arrangement is used for all five cathode materials. A process for identifying critical diffusivity and conductivity values using global sensitivity analysis is established as follows. The simulation results are sorted according to diffusivity magnitude, and a succession of data sub-sets are compiled for an increasingly narrower diffusivity range by increasing the lower bound. Independent surrogate models are constructed at each stage, and used to compute global sensitivity indices. In this manner, the critical value can be identified when the impact of diffusivity vanishes for a given lower bound. Figure 3 shows that for all materials besides lithium titanium sulfide, the effect of diffusivity is dwarfed by either conductivity or cycling rate. For lithium titanium sulfide, however, the effect of diffusivity is significant over the full range, and gradually decreases until becoming negligible at about $2.4 \times 10^{-15} \text{ m}^2/\text{s}$. Since diffusivity can be determined as a function of lithium ion concentration⁴⁵ and voltage,⁴⁶ quantifying this critical value establishes a benchmark to aim for when designing or processing materials with similar chemistry. The global sensitivity

Table III. Fixed parameter values for cell simulations.

Parameter	Value
Initial stoichiometric parameter for anode (x in Li _x C ₆)	0.8
Initial stoichiometric parameter for cathode (y in Li _y Mn ₂ O ₄ , etc.)	0.1
Anode thickness	100 μm
Cathode thickness	100 μm
Separator thickness	25 μm
Positive current collector thickness	25 μm
Negative current collector thickness	25 μm
Ambient temperature	298 K
Diffusion coefficient in anode	$5.0 \times 10^{-13} \text{ m}^2/\text{s}$
Electrical conductivity in anode	100 S/m
Diffusion coefficient in electrolyte	$5.34 \times 10^{10} e^{-0.65c} \text{ m}^2/\text{s}$
Ion conductivity in electrolyte	$0.0911 + 1.91c - 1.05c^2 + 0.155c^3$
Particle size in anode	10 μm
Volume fraction of inert filler in cathode	0.2
Volume fraction of electrolyte in cathode	0.3
Volume fraction of inert filler in anode	0.1
Volume fraction of electrolyte in anode	0.3
Electrolyte	LiPF ₆ in EC:DMC
Initial salt concentration	1000 mol/m ³
Density of electrolyte	1324 kg/m ³
Density of inert filler	1800 kg/m ³

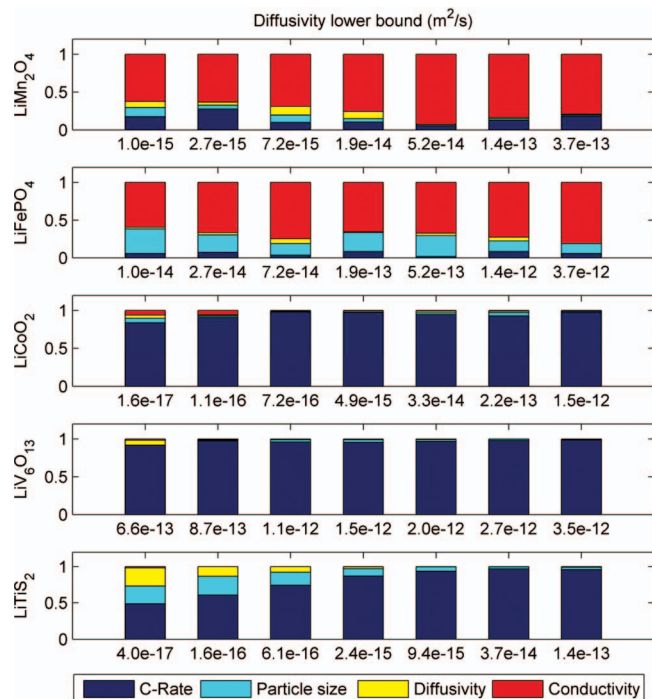


Figure 3. Main sensitivity indexes for various diffusivity ranges.

analysis results also demonstrate that in most cases, adequate cell energy performance can be achieved so long as conditions independent of the diffusivity are satisfied.

A similar analysis is performed for conductivity and the results are plotted in Figure 4. In the case of lithium cobalt oxide, lithium vanadium oxide, and lithium titanium sulfide, the lower bound for conductivity is sufficiently high to not significantly affect the cell performance. However, for lithium manganese oxide and lithium iron phosphate, conductivity is found to have a strong effect on performance, and critical values of about 0.01 S/m and 0.2 S/m are identified, respectively.

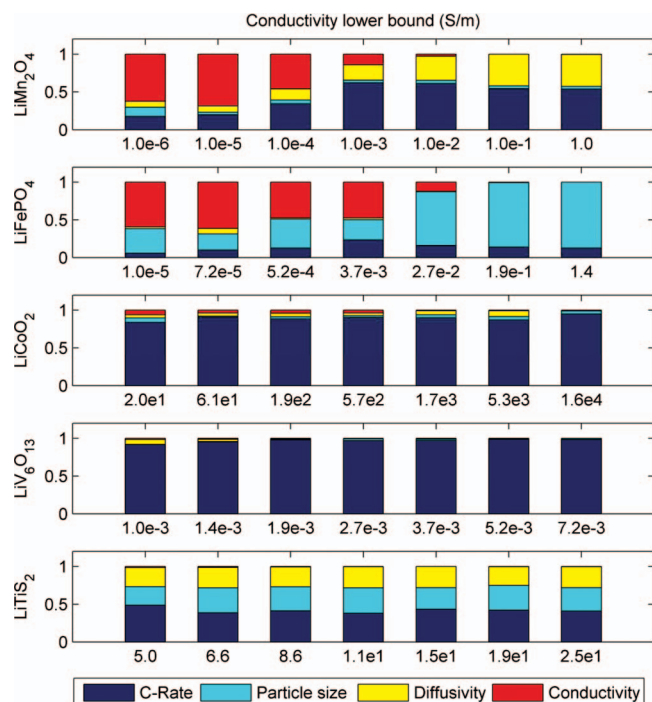


Figure 4. Main sensitivity indexes for various conductivity ranges.

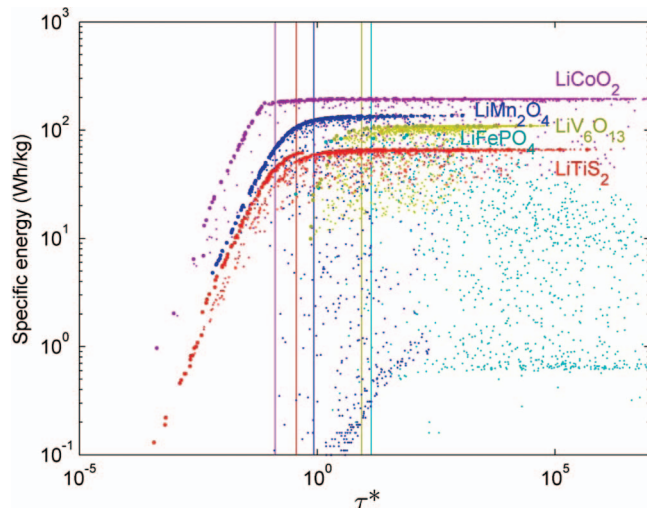


Figure 5. Separation of operating regimes based on dimensionless time.

quantified, respectively. Again, quantification of these values can provide guidelines for processing and manufacturing. For instance, these results, in conjunction with recent progress in modeling the influence of additives on conductivity,⁴⁷ can be used to optimize the amount of conductive additive to introduce to the undoped cathode material.

Dimensionless parameterization.— Although the input variables are treated as being independent in the design of experiments, their effects within the battery cell are coupled. It is reasonable, then, to seek a way to combine the variables in a more efficient manner in order to reduce the problem dimensionality. This can be done by performing dimensional analysis, in which the output is modeled not as a function of independent input variables, but as a function of newly defined dimensionless parameters that combine multiple physical variables. Dimensional analysis has been used previously to compare characteristic diffusion and discharge time scales for lithium manganese oxide,⁴⁸ and is also widely used in fields such as fluid mechanics and heat transfer for characterization and scaling analysis.⁴⁹

The diffusivity $D_{s,p}$ has dimensions of length squared divided by time, and appears as a coefficient in Eq. 4, whose corresponding length scale is the particle radius $R_{s,p}$. These two variables can be combined to yield a characteristic time scale for the diffusion equation.

$$t_{\text{diffusion}} = \frac{R_{s,p}^2}{D_{s,p}} \quad [5]$$

Another important time scale is the time required to discharge the cell, which is estimated from the definition of cycling rate.

$$t_{\text{discharge}} = \frac{k}{C} \quad [6]$$

The constant $k = 3600$ seconds/hour ensures that the two length scales have consistent units. We can thus define a dimensionless time parameter τ^* as the ratio of the two time scales.

$$\tau^* = \frac{t_{\text{discharge}}}{t_{\text{diffusion}}} = \frac{k D_{s,p}}{C R_{s,p}^2} \quad [7]$$

Physically, τ^* represents the relative speed of the diffusion and discharge processes. When the magnitude of τ^* is very large, ions travel much faster through the particle via diffusion than they are transferred across the cell. Conversely, when the magnitude of τ^* is very small, the cell utilization is limited by the diffusion rate. A log-scale plot of the computed specific energy against τ^* is shown in Figure 5.

Aside from significant scatter in the data, two distinct regions can be identified in Figure 5: the maximum achievable specific energy increases monotonically in the low- τ^* range up to some critical point,

beyond which it remains roughly constant. Performance in the low- τ^* region is limited by poor ion transport via diffusion causing a depletion of salt in the electrolyte. This can be observed for three of the materials (LiMn_2O_4 , LiCoO_2 , and LiTiS_2), although the maximum energy levels differ. The boundary between these two operating regimes can be considered a critical point that must be satisfied when conducting cell design. In order to quantify this critical point, we consider the Pareto front, or the set of Pareto-efficient solutions for each variable. A solution is considered Pareto-efficient if it is not dominated by any other solution in the data set; that is, if there is no other point in the data set that is better in all objective functions.⁵⁰ By defining the two objectives as maximizing specific energy and minimizing τ^* , the data are divided into the Pareto front consisting of solutions forming the clear maximum-energy curves in Figure 5, and the remainder which form the scatter in the data.

The critical point can be defined as the minimum value of τ^* such that the (log-scale) slope of the Pareto front becomes less than some tolerance δ .

$$\tau_{crit}^* = \min(\tau^*) \left| \frac{dy}{dx_1} \right| < \delta \quad [8]$$

$$y \equiv \log_{10} E_{cell} \quad [9]$$

$$x_1 \equiv \log_{10} \tau^* \quad [10]$$

Using the definitions for transforming the specific energy e and the dimensionless time parameter τ^* in Eqs. 9 and 10, respectively, the slope of the Pareto front is estimated using the central-difference scheme.

$$\left. \frac{dy}{dx_1} \right|_{x_{1,n}} \approx \frac{y_{n+1} - y_{n-1}}{x_{1,n+1} - x_{1,n-1}} \quad [11]$$

The critical values of τ^* calculated using Eqs. 8–11 are plotted as vertical lines in Figure 5. A tolerance value of $\delta = 0.1$ is used for all materials.

The dimensionless parameter that we defined in Eq. 7 combines three of the four variables into a single parameter that can be used to predict cell performance without needing to conduct a full cell simulation. However, two materials ($\text{LiV}_6\text{O}_{13}$ and LiFePO_4) did not demonstrate a clear separation of operating regimes based on τ^* . We note that one final input variable has been excluded from this definition, the conductivity. Since conductivity is the inverse of resistivity, by Ohm's law it has dimensions of electrical current per unit voltage, per unit length. Therefore, a dimensionless conductivity parameter can be defined as in Eq. 12, where the reference voltage V_{co} is the cell potential at the end of discharge, the reference current I_0 is the discharge current, and the characteristic length scale L_+ is the electrode thickness.

$$\sigma^* = \frac{\sigma V_{co}}{I_0 L_+} \quad [12]$$

The parameter σ^* can be interpreted as a ratio of the material's conductivity to the required conductivity for transporting electrons at the rate dictated by the discharge current. When the magnitude of this ratio is very small, the cell performance can be expected to be limited by conductivity. A plot of specific energy with respect to σ^* in Figure 6 shows that two distinct operating regimes can again be identified for some materials, including $\text{LiV}_6\text{O}_{13}$ and LiFePO_4 . Referring to the variable bounds listed in Table I, we note that the diffusivity lower bounds for these two materials are much higher than for the others. This suggests that within the selected parameter space, the performance of $\text{LiV}_6\text{O}_{13}$ and LiFePO_4 is limited by conduction but not diffusion. Similarly, Figure 6 shows that the relatively high conductivity range for LiCoO_2 and LiTiS_2 results in little variation in cell performance as σ^* is varied.

Critical values are also plotted in Figure 5, based on the definition in Eqs. 13 and 14 applied to the set of points in the Pareto front.

$$\sigma_{crit}^* = \min(\sigma^*) \left| \frac{dy}{dx_2} \right| < \delta \quad [13]$$

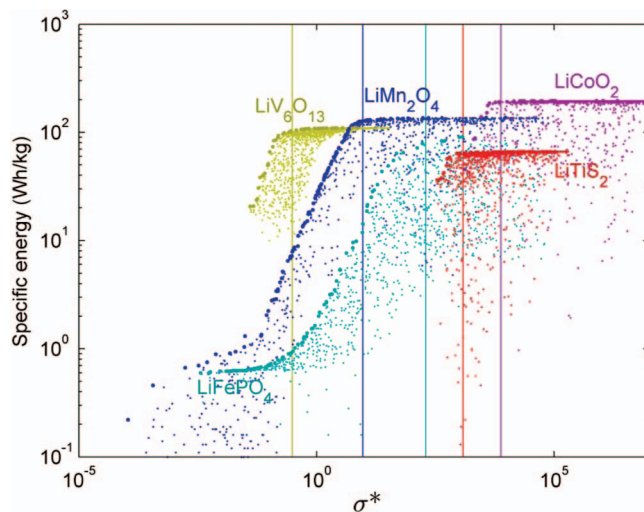


Figure 6. Separation of operating regimes based on dimensionless conductivity.

$$x_2 \equiv \log_{10} \sigma^* \quad [14]$$

The same central-difference scheme is used to estimate the derivative, and the same tolerance of $\delta = 0.1$ is used.

$$\left. \frac{dy}{dx_2} \right|_{x_{2,n}} \approx \frac{y_{n+1} - y_{n-1}}{x_{2,n+1} - x_{2,n-1}} \quad [15]$$

Dimensionless energy function.— We have identified two dimensionless parameters that characterize the conditions under which cell performance is limited by diffusivity and conductivity. It is reasonable, therefore, to combine them in a way that accounts for the limiting effects of both processes. We begin by defining in Eq. 16 a new parameter x^* as the base-10 logarithm of the lesser of the two dimensionless parameters for each data point.

$$x^* \equiv \log_{10} (\min[\sigma^*, \tau^*]) \quad [16]$$

Physically, this corresponds to the numerical value corresponding to the most limiting dimensionless transport parameter. We then consider the Pareto front discussed in the previous section, which represents the maximum achievable energy performance of a cell for the specified dimensionless diffusivity and conductivity range. We have noted in Figures 5 and 6 a distinctive shape for the Pareto front, so it makes sense to attempt to define this shape using a mathematical curve fit. First, we non-dimensionalize the energy density using Eq. 17 in order to obtain a curve fit that is entirely free of dimensional units.

$$\varepsilon^* = \frac{E_{cell} m_{battery}}{Q V_0 m_{active}} \quad [17]$$

In this case, the energy density of the cell is normalized by the limiting capacity Q , initial cell voltage V_0 , and the mass ratio of active to total materials in the cell. The limiting capacity is defined as the lesser of the two electrode capacities based on the electrode thicknesses and values listed in Table II, and the active mass includes both electrodes. The curve fit can be obtained using the surrogate modeling techniques described in the methodology, but in this case we desire a more specific class of functions that have asymptotic bounds at their infinite limits. To characterize the dimensionless energy function in Eq. 17 with respect to the parameter x^* , we use the generalized logistic function given in Eq. 18.

$$\hat{\varepsilon}^* = \frac{k_1}{1 + k_2 e^{-k_3 x^*}} + k_4 \quad [18]$$

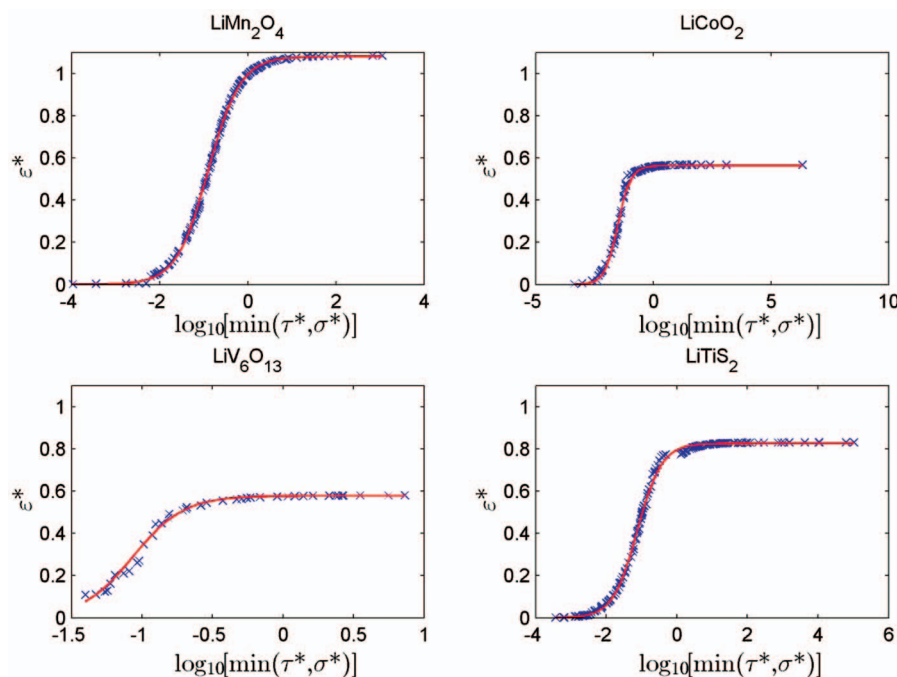


Figure 7. Generalized logistic function fitted for the Pareto-efficient set of each material.

This class of functions has been used in growth modeling,⁵¹ as its constants govern the shape of the curve in easily identifiable ways. It is readily applicable here as the energy curves shown in Figs. 5 and 6 share similar characteristics. In the limit as x^* approaches negative infinity, the exponential term in the denominator becomes unbounded, and thus the lower asymptote is equal to k_4 . In our case, this corresponds to the limit of zero diffusivity and zero conductivity, so for physical consistency we require $k_4 = 0$, and consider a form of the generalized logistic function with only three constants.

$$\hat{\varepsilon}^* = \frac{k_1}{1 + k_2 e^{-k_3 x^*}} \quad [19]$$

In the infinite limit in the opposite direction, the exponential term vanishes and the function value reaches the upper limit value k_1 . The remaining constants k_2 and k_3 govern the growth rate and location of growth, respectively. The three constants are determined by minimizing the curve fit prediction error, defined in Eq. 20 as the sum of the differences between the exact and approximate dimensionless energy function values given in Eqs. 17 and 19, respectively. This is implemented using the MATLAB function `fminunc`.

$$\text{error} = \sum_{i=1}^{x_p} |\varepsilon_i^* - \hat{\varepsilon}_i^*| \quad [20]$$

Plots of the fitted generalized logistic functions along with the Pareto-efficient set for each material are shown in Fig. 7, and the constants governing their shapes are given in Table IV, along with mean prediction errors. Note that LiFePO_4 is not considered in this analysis, as its Pareto-efficient set contains an insufficient number of points to conduct a meaningful curve fit or error analysis. However, we notice that for the remaining materials, the generalized logistic function provides an excellent description of the maximum achievable

energy performance, with mean prediction errors typically about 1% of the normalized function value or less.

Finally, it is useful to convert the maximum dimensionless energy (i.e., the k_1 value for each material) to physical quantities to compare these results with theoretical predictions and experimental measurements. Our energy density values are generally lower than expected; for example, the values of 195.6 Wh/kg for LiCoO_2 and 136.3 Wh/kg for LiMn_2O_4 obtained in this study are much lower than the respective theoretical limits of 272.1 Wh/kg and 223.2 Wh/kg for jellyroll format batteries.¹⁰ Similarly, the maximum value of 109.8 Wh/kg for $\text{LiV}_6\text{O}_{13}$ is much lower than the 200–300 Wh/kg estimate for a thin film battery reported by Munshi and Owens.⁵² For LiTiS_2 , the energy density value of 66.2 Wh/kg is within 11% of the 73 Wh/kg reported by Brandt.⁵³

There are two main reasons for these discrepancies. First, as shown in Table III, the full state-of-charge (SOC) window is not utilized in these simulations. This was done for numerical reasons, as good data for the open circuit potential are not available at very high and very low SOC for some materials, and a consistent SOC window is necessary to ensure a consistent comparison of the materials. Second, the simulations use fixed anode properties instead of scaling them with the cathode properties to match capacity, and no optimization is performed. Again, this was done to ensure a consistent comparison, resulting in some loss in cell performance. Despite these simplifications, the relative cell-level energy density values are found to be consistent with the materials' electric potential and capacity.

Conclusions

In this study we applied a surrogate modeling framework to perform global sensitivity analysis with respect to diffusivity and conductivity for several different Li-ion cathode materials, and identified two dimensionless parameters that characterize the cell performance by combining multiple input variables and fixed quantities. Critical values for both the physical and dimensionless parameters were quantified, yielding benchmark numbers that may aid in cell design. For example, insight into the effect of diffusivity under a wide range of cycling rates established in this study can provide guidelines for material processing to achieve the desired particle size distribution. Similarly, the quantification of critical conductivity levels can help

Table IV. Generalized logistic functions and their mean prediction errors.

	LiMn_2O_4	LiCoO_2	$\text{LiV}_6\text{O}_{13}$	LiTiS_2
k_1	1.080	0.563	0.578	0.826
k_2	0.0864	0.0045	0.0028	0.0398
k_3	2.737	3.585	5.535	2.887
Mean error	0.0056	0.0084	0.0107	0.0081

determine the optimal amount of conductive additives to introduce in the manufacturing process.⁴⁷

In addition, dimensional analysis was applied to identify two dimensionless parameters to characterize the energy performance of the cell. Despite significant differences in capacity and transport properties, all electrode materials showed a similar performance dependence on the two dimensionless parameters. Since these two parameters can be interpreted as ratios of transport rates (diffusivity and conductivity) to cell operating conditions (cycling rate and discharge current), these results suggest that for all cathode materials considered, ion transport via diffusion and electron transport via conduction are the two most critical limitations to cell performance. The critical points where cell performance becomes independent of the dimensionless parameters were also quantified, and found to be close to unity for all materials. This is again consistent with our physical interpretation that unity represents the point at which all transport rates are balanced with the cell operation. By combining the two dimensionless transport parameters into a single quantity, and non-dimensionalizing the energy density as well, a generalized logistic function was shown to describe the Pareto front well for all materials except LiFePO₄, which had a Pareto-efficient set of insufficient size. The generalized logistic function obtained in this study can be considered a type of reduced-order model, in which the maximum energy performance of a cell can be readily estimated with an analytical equation based on the material properties and composition of the electrodes, and the operational parameters of the cell.

Although maximum energy density values in this study are generally lower than theoretical limits, they are consistent with the relative voltage and capacity of the materials. Since they are valid for all of the materials considered in this study, the dimensionless relationships established here can also provide guidelines for designing new materials with tunable properties. It should also be noted that all analysis performed in this study was based on a macroscopic homogeneous cell model and thus does not account for electrode morphology, which has been found to significantly affect effective transport properties.⁵⁴ Current efforts are being made toward implementing a multi-scale model that can more accurately capture the physical phenomena in a cell, while remaining feasible for conducting a large number of simulations for surrogate modeling.

Acknowledgments

The present efforts have been supported by the General Motors and University of Michigan Advanced Battery Coalition for Drivetrains (ABCD).

References

1. M. Park, X. Zhang, M. Chung, G. B. Less, and A. M. Sastry, *J. Power Sources*, **195**, 7904 (2010).
2. C.-H. Lu and S.-W. Lin, *J. Power Sources*, **97**, 458 (2001).
3. T. Drezen, N.-H. Kwon, P. Bowen, I. Teerlinck, M. Isono, and I. Exnar, *J. Power Sources*, **174**, 949 (2007).
4. T. D. Tran, J. H. Feikert, R. W. Pekala, and K. Kinoshita, *J. Appl. Electrochem.*, **26**, 1161 (1996).
5. R. E. Garcia, Y.-M. Chiang, W. C. Carter, P. Limthongkul, and C. M. Bishop, *J. Electrochem. Soc.*, **152**, A255 (2005).
6. R. Darling and J. Newman, *J. Electrochem. Soc.*, **144**, 4201 (1997).
7. S. Ahn, Y. Kim, K. J. Kim, T. H. Kim, H. Lee, and M. H. Kim, *J. Power Sources*, **81**, 896 (1999).
8. J. Cho, H. Kim, and B. Park, *J. Electrochem. Soc.*, **151**, A1707 (2004).
9. D. D. MacNeil, Z. Lu, Z. Chen, and J. R. Dahn, *J. Power Sources*, **108**, 8 (2002).
10. W. F. Howard and R. M. Spotnitz, *J. Power Sources*, **165**, 887 (2007).
11. M. Doyle and J. Newman, *J. Appl. Electrochem.*, **27**, 846 (1997).
12. W. Shyy, Y. C. Cho, W. Du, A. Gupta, C. C. Tseng, and A. M. Sastry, *Acta Mech. Sin.*, **27**, 845 (2011).
13. X. Zhang, A. M. Sastry, and W. Shyy, *J. Electrochem. Soc.*, **155**, A542 (2008).
14. A. Gupta, J. H. Seo, X. Zhang, W. Du, A. M. Sastry, and W. Shyy, *J. Electrochem. Soc.*, **158**, A487 (2011).
15. M. Doyle, J. Newman, A. S. Gozdz, C. N. Schmutz, and J.-M. Tarascon, *J. Electrochem. Soc.*, **143**, 1890 (1996).
16. S. Yu, Y. Chung, M. S. Song, J. H. Nam, and W. I. Cho, *J. Appl. Electrochem.*, **42**, 443 (2012).
17. N. V. Queipo, R. T. Haftka, W. Shyy, T. Goel, R. Vaidyanathan, and P. K. Tucker, *Prog. Aero. Sci.*, **41**, 1 (2005).
18. M. D. McKay, R. J. Beckman, and W. J. Conover, *Technometrics*, **21**, 239 (1979).
19. R. H. Myers and D. C. Montgomery, *Response Surface Methodology: Process and Product in Optimization Using Designed Experiments*, Wiley and Sons Inc., New York (1995).
20. S. N. Lophaven, H. B. Nielsen, and J. Sondergaard, *DACE—A Matlab kriging toolbox*. Version 2.0, Technical Report, IMM-TR-2002-12, Technical University of Denmark, Denmark, 2002.
21. T. Goel, D. J. Dorney, R. T. Haftka, and W. Shyy, *Comput. Fluids*, **37**, 705 (2008).
22. I. Sobol, *Math. Model. Comput. Exp.*, **4**, 407 (1993).
23. A. Yamada, H. Koizumi, S. Nishimura, N. Sonoyama, R. Kanno, M. Yonemura, T. Nakamura, and Y. Kobayashi, *Nature Mat.*, **5**, 357 (2006).
24. K. West, B. Zachau-Christiansen, and T. Jacobsen, *Electrochim. Acta*, **28**, 1829 (1983).
25. D. Guyomard and J. M. Tarascon, *J. Electrochem. Soc.*, **140**, 3071 (1993).
26. M. Y. Saidi, J. Barker, and R. Koksang, *J. Solid State Chem.*, **122**, 195 (1996).
27. K. Dokko, M. Nishizawa, M. Mohamedi, M. Umeda, I. Uchida, J. Akimoto, Y. Takahashi, Y. Gotoh, and S. Mizuta, *Electrochem. Solid-State Lett.*, **4**, A151 (2001).
28. F. Cao and J. Prakash, *Electrochim. Acta*, **47**, 1607 (2002).
29. J. Marzec, K. Swierczek, J. Przewoznik, J. Molenda, D. R. Simon, E. M. Kelder, and J. Schoonman, *Solid State Ionics*, **146**, 225 (2002).
30. J. R. Dygas, M. Kopec, F. Krok, D. Lisovyskiy, and J. Pielaszek, *Solid State Ionics*, **158**, 2153 (2005).
31. M. Gaberscek, R. Dominko, and J. Jamnik, *Electrochem. Comm.*, **9**, 2778 (2007).
32. R. Amin, P. Balaya, and J. Maier, *Electrochem. Solid-State Lett.*, **10**, A13 (2007).
33. R. Amin, C. Lin, and J. Maier, *Phys. Chem. Chem. Phys.*, **10**, 3524 (2008).
34. S. L. Bewlay, K. Konstantinov, G. X. Wang, S. X. Dou, and H. K. Liu, *Mater. Lett.*, **58**, 1788 (2004).
35. S. H. Choi, J.-W. Son, Y. S. Yoon, and J. Kim, *J. Power Sources*, **158**, 1419 (2006).
36. A. Van der Ven and G. Ceder, *Electrochem. Solid-State Lett.*, **3**, 301 (2000).
37. J. Xie, N. Imanishi, T. Matsumura, A. Hirano, Y. Takeda, and O. Yamamoto, *Solid State Ionics*, **179**, 362 (2008).
38. Y. I. Jang, B. J. Neudecker, and N. J. Dudney, *Electrochem. Solid-State Lett.*, **4**, A74 (2001).
39. Y. Takahashi, N. Kijima, K. Tokiwa, T. Watanabe, and J. Akimoto, *J. Phys.: Condens. Matter*, **19**, 436202 (2007).
40. G. Pistoia, M. Pasquali, Y. Geronov, V. Manev, and R. V. Moshtev, *J. Power Sources*, **27**, 35 (1989).
41. C. Lampe-Onnerud, J. O. Thomas, M. Hardgrave, and S. Yde-Andersen, *Solid State Ionics*, **81**, 189 (1995).
42. P. C. Spurdens and B. C. H. Steele, *Solid State Ionics*, **21**, 151 (1986).
43. D. Zehnder, C. Deshpande, B. Dunn, and R. F. Bunshah, *Solid State Ionics*, **18-19**, 813 (1986).
44. C. Julien, I. Samaras, O. Gorochoy, and A. M. Ghorayeb, *Phys. Rev. B*, **45**, 390 (1992).
45. A. Van der Ven, J. C. Thomas, Q. Xu, B. Swoboda, and D. Morgan, *Phys. Rev. B*, **78**, 104306 (2008).
46. G. B. Less, J. H. Seo, S. Han, A. M. Sastry, J. Zausch, A. Latz, S. Schmidt, C. Wieser, D. Kehrwald, and S. Fell, *J. Electrochem. Soc.*, **159**, A697 (2012).
47. M. Zhu, J. Park, and A. M. Sastry, *J. Electrochem. Soc.*, **158**, A1155 (2011).
48. W. Du, A. Gupta, X. Zhang, A. M. Sastry, and W. Shyy, *Int. J. Heat Mass Transfer*, **53**, 3552 (2010).
49. H. L. Langhaar, *Dimensional Analysis and Theory of Models*, Wiley and Sons Inc., New York (1951).
50. Y. Mack, T. Goel, W. Shyy, and R. Haftka, *Studies in Computational Intelligence*, **51**, 323 (2007).
51. F. J. Richards, *J. Exp. Bot.*, **10**, 290 (1959).
52. M. Z. A. Munshi and B. B. Owens, *Solid State Ionics*, **38**, 87 (1990).
53. K. Brandt, *Solid State Ionics*, **69**, 173 (1994).
54. B. Vijayaraghavan, D. R. Ely, Y.-M. Chiang, R. Garcia-Garcia, and R. E. Garcia, *J. Electrochem. Soc.*, **159**, A548 (2012).